Microfluid Nanofluid (2016) 20:160
DOI 10.1007/s10404-016-1826-y

RESEARCH PAPER

An experimental characterization of a tunable separation device

E. J. Mossige[1,2] · A. Jensen[1] · M. M. Mielnik[3]

Received: 1 August 2016 / Accepted: 8 November 2016 / Published online: 16 November 2016
© Springer-Verlag Berlin Heidelberg 2016

Abstract By the use of an experimental setup for microfluidic flows, we have characterized the separation and concentration characteristics of the so-called Trilobite™ separation unit. Our separation unit consists of microfluidic channels and an elliptical separation geometry with a solid and a permeable wall region. We show that it is possible to adjust the thickness of different flow layers by changing the flow rates and pressure drop over the permeable wall. For high pressure drops, the separator shows promising concentration characteristics. For low pressure drops, an increase in flow rate results in a thinning of the flow layers. For sufficiently high flow rates, it should therefore be possible to create flow layers sufficiently thin that the particle separation is entirely dominated by hydrodynamic forces. This, in turn, will enable clog-free particle separation.

Keywords Particle separation · Concentration · Particle image velocimetry · Clog-free · Permeable wall

The original article was revised: The sentence "Mean flow is from right to left." in caption of Fig. 7 was incorrect. This sentence has been corrected.

✉ E. J. Mossige
endrejm@math.uio.no

[1] Department of Mathematics, University of Oslo, 0851 Oslo, Norway

[2] Trilobite Microsystems, 4630 Kristiansand, Norway

[3] Department of Microsystems and Nanotechnology (MiNaLab), SINTEF ICT, Gaustadalleen 23C, 0373 Oslo, Norway

1 Introduction

Water scarcity is one of mankind's biggest challenges: around 748 million individuals do not have access to a clean drinking water source [WWAP (United Nations World Water Assessment Programme) 2015] and the access is becoming more and more limited (WHO/UNICEF Joint Monitoring Programme for Water Supply and Sanitation 2004). This development is accelerated by a growing population and increased agricultural activity. Thus, processes to treat water for reuse, known as water treatment, are called for (Jhansi and Mishra 2013).

A crucial step in any water treatment process is the separation of particles. In the industry, conventional separation methods are most common. These are filtration, sedimentation and centrifugation (Grandison and Lewis 1996). Dead-end filters are the most common industrial filters. In a dead-end filter, only particles smaller than the pore size can pass through the filter. Large particles are collected in the filter, forming a cake that reduces the effective pore size. Eventually, the filter clogs and has to be changed or cleaned.

The ability to separate, sort and concentrate particles is important also in many miniaturized systems, e.g. for medical diagnostics (Rivet et al. 2011). In miniaturized systems applications, such as lab-on-a-chip systems, a distinction is usually made between discrete and continuous particle separation (Pamme 2007). In the former case, particles are separated one by one, whereas in the latter case, they are separated in a continuous manner, enabling e.g. high throughput.

In continuous hydrodynamic separation, the separation of particles is performed with no external force field to manipulate the migration of particles (Karimi et al. 2013). Only hydrodynamic forces act on the particles. These types of systems have certain advantages over other types of separation methods, such as electrophoresis, flow cytometry, and separation by thermal forcing (Zhu and Ye 2010; Zhu

et al. 2011; Nabeth et al. 2010). These advantages include scalability, high throughput and ease of implementation on chips for complete micro total analysis systems. Another advantage is integrability into larger processing systems with both upstream and downstream processes. Unfortunately, continuous hydrodynamic separation methods suffer from low pureness of the processed particle streams and poor handling of liquids with high-particle concentrations. Yet, the main shortcoming of most of these techniques is their tendency to clog. This is especially true for microfilters, which is the most commonly used separation technique in microfluidic systems.

Microfilters can be divided into two main types. In the first type the side channels are tangent to the main channel. This is known as crossflow filtration. The side channel width is either made smaller than the smallest particle in the suspension or large enough to allow for particles below a threshold dimension to enter Lenshof and Laurell (2010). These types of filters are easy to manufacture, but suffer from clogging. To reduce the tendency to clog, Mielnik et al. (2005) suggested a method to increase the shear force tangent to the main channel, at the side channel inlets. In the other type of microfiltration, known as hydrodynamic filtration, the fact that particles have a tendency to follow the stream which has the highest flow rate is used to separate the particles (Svanes and Zweifach 1968). This is known as the Zweifach–Fung effect. This method was first used to separate particles in microchannels by Yamada and Seki (2005), who successfully separated polymer microspheres based on the sphere diameter. In addition, the method was verified for selective enrichment of leukocytes from blood without signs of clogging. Hydrodynamic filtration is now commonly used to concentrate blood samples (Jäggi et al. 2007).

Microfluidic flows have been analyzed by several authors (Meinhart et al. 1999, 2000; Park et al. 2004; Kolaas et al. 2013), but to the best of our knowledge, little work is done on the analysis of the flows inside microseparators. Exceptions are Sugaya et al. (2011) and Eea (2014) who used particle image velocimetry (PIV) to characterize a separation device for non-spherical rigid particles and for non-spherical soft particles, respectively. Recently, Hood et al. (2016) used PIV to measure particle migration characteristics for inertial flows in microchannels.

The Trilobite™ separation microchip presented in this paper was initially developed for the concentration of cancer (CaSki) cells studied by Dong et al. (2011), who performed design evaluation by means of numerical simulations and initial functionality tests. The same device has also been used for the pre-concentration of microalgae (Hönsvall et al. 2016) according to size. These authors demonstrated the overall performance potential, however, no detailed hydrodynamic analysis attempting to explain the observed performance has been reported previously to the authors' knowledge. In this paper, we present a thorough analysis of the flow field through the separation device. We performed experiments for different flow rates and pressure drops inside the microfluidic channels to characterize the hydrodynamic separation and concentration functionality of the Trilobite separator. By extracting streamlines, streaklines, and velocity fields by the use of a micro-PIV setup, we found that the microchip can be operated either as a conventional filter or a potentially clog-free hydrodynamic separator. The operational modes of the device depend on the inlet and outlet conditions of the chip; we show how these conditions can be controlled to achieve the best possible separation performance, and propose important design improvements. Lastly, we explain why low flow rates lead to high concentration ratios, as observed by Dong et al. (2011).

2 Working principle

The working principle of the microfluidic separator is presented in Fig. 1a. The trilobite shaped separation unit consists of a bluff body, pillars that make up a permeable wall and an outlet for the permeate flow. The pillars are separated by a distance $l = 25\,\mu\text{m}$ and make up a permeable wall. The flow that enters the pores between the pillars and exits through the permeate outlet is called the permeate flow. The thickness of this flow layer is T_p, see Fig. 1. The flow outside this layer continues downstream to a concentrate outlet and is therefore called the concentrate flow. The blue particles are brought downstream by this flow.

The thickness T_p is dictated by the position of the saddle point downstream of the trilobite structure. When the saddle point is in an upstream position, close to the trilobite structure, T_p is small and when the saddle point is in a downstream position, T_p is large. The saddle point position is used to determine the working mode of the unit because when T_p is larger than the pore size, $T_p > l$, the separator works as a dead-end or crossflow filter. In this case, the pillars serve to prevent particles with diameter larger than the pore size l from entering the permeate outlet. With this configuration, the cut-off size of particles is determined mechanically by the pore size l, and not by the permeate flow layer T_p. When instead the saddle point is brought sufficiently far upstream that $T_p < l$, the cut-off size is determined by T_p, and not by l. With this flow configuration, the separator works as a hydrodynamic filter and is potentially clog-free because only particles smaller than T_p are allowed to enter the permeate flow region.

Velocity shear inside the boundary layer along the separation unit might also affect the separation of particles. This is because the velocity shear inside this layer gives rise to

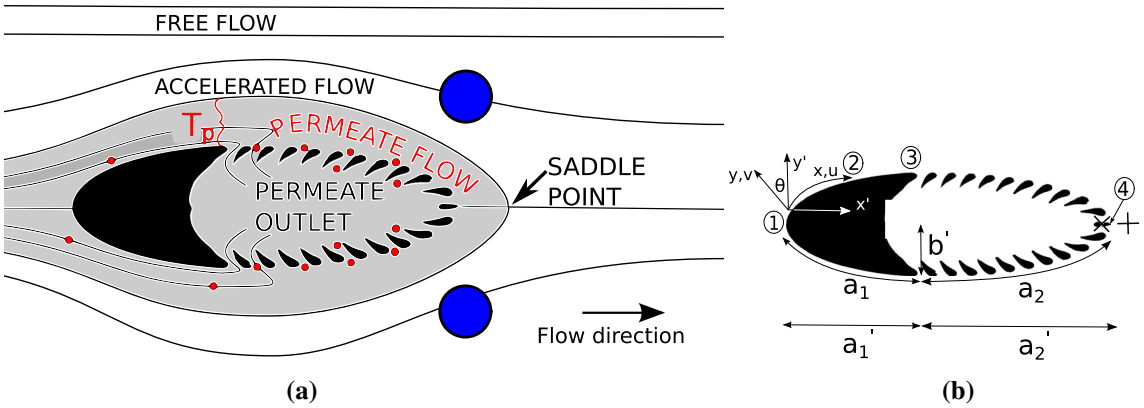


Fig. 1 **a** Hydrodynamic filtration principle as used by the separator. The *red particles* are the passive tracer particles that faithfully follow the streamlines of the undisturbed flow. The *large blue* particles have their center outside the permeate flow layer T_p and are therefore separated and continue downstream to the concentrate outlet. The saddle point position determines T_p: an upstream saddle point leads to a small T_p, and a downstream saddle point leads to a large T_p. **b** Local coordinate system (x, y) and global coordinate system (x', y'). The streamwise coordinates x and x' start from the stagnation point at 1 and ends at 4, which is at the downstream tip of the structure. The upstream saddle point is marked by 'X' (30 μm upstream of 4), and the downstream saddle point is marked by '+' (90 μm downstream of 4). The length of the solid wall region along x and x' are $a_1 = 532\,\mu\text{m}$ and $a_1' = 442.8\,\mu\text{m}$, respectively. Along the permeable wall region, the corresponding lengths are $a_2 = 772\,\mu\text{m}$ and $a_2' = 694.3\,\mu\text{m}$, respectively. The half width is $b' = 229.5\,\mu\text{m}$ (color figure online)

normal forces on particles. One such force is the Saffman lift force (Saffman 1965). The thickness of the boundary layer is denoted by T_{bl}.

3 Experiments

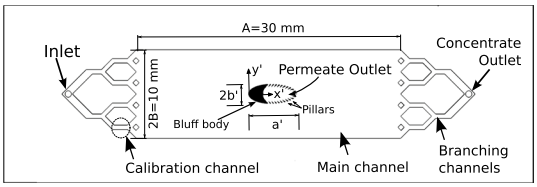
3.1 Fabrication of microfluidic chips

The microfluidic chips were fabricated at SINTEF MiNaLab's ISO certified MEMS fabrication facilities. Briefly, a six inch Silicon-on-insulator (SOI) wafer with 380 μm handle wafer, 500 nm BOX and 90 μm device layer was thermally oxidized, coated by photoresist, and patterned using a mask containing the layout of the microfluidic channels and the separator (Trilobite™) structure. The pattern was then transferred to the SiO_2 hardmask by reactive ion etch, and the fluidic structures were etched in the device layer of the SOI wafer by Deep Reactive Ion Etch (DRIE) using the BOX as stop layer, resulting in a uniform depth of 90 μm for all fluidic channels. The permeate outlets were realized by patterning and DRIE etching the backside (i.e. handle wafer side) of the wafers using back side alignment of the mask with accuracy of ±2μm and similar process steps as for device layer patterning. Finally, the oxide (and BOX) was stripped by wet etching, a glass wafer (300 μm thickness) was bonded on the device layer side of the SOI wafer to seal the microfluidic channels, and the wafer was diced into individual chips. The microchip used in the experiments is shown in Fig. 2a. It consists of an inlet and concentrate outlet interconnected by microfluidic channels. We wanted to study the flow around the separator with minimal influence from inlets and outlets as well as from side walls. Therefore, the main channel was $A = 30$ mm long and $2B = 10$ mm wide, which is large compared to the separation unit (1137 μm long and 459 μm wide).

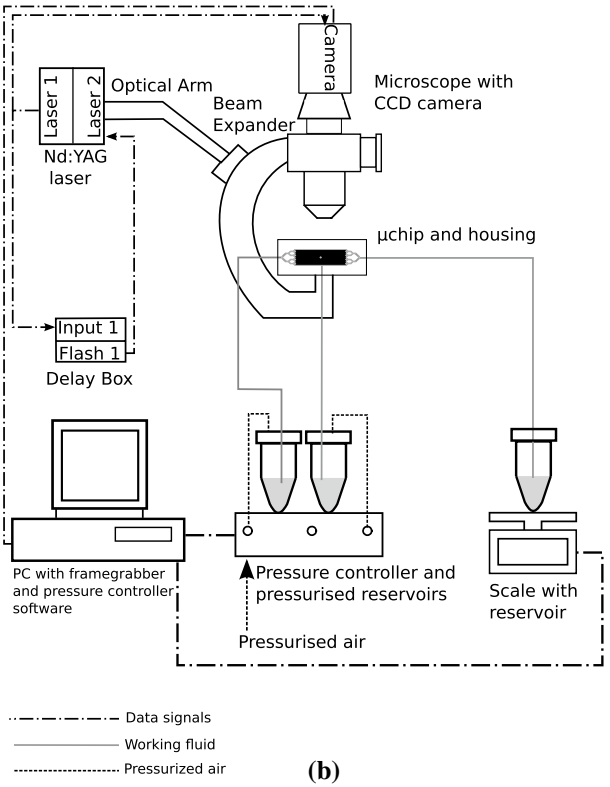
A detail view of the separation unit and the local coordinate system is shown in Fig. 1b. The arc length of the unit along the local streamwise coordinate x is $a = a_1 + a_2 = 1305\,\mu\text{m}$ and the dimensionless streamwise coordinate is $\tilde{x} = x/a$, with $0 < \tilde{x} < 1$ The solid wall region from position ① to v has length $a_1 = 532\,\mu\text{m}$ and the permeable wall region from v to ④ has length $a_2 = 772\,\mu\text{m}$. At v, the streamwise coordinate is $\tilde{x} = 0.408$. The length of the solid wall region along the global streamwise coordinate x' is $a_1' = 442.8\,\mu\text{m}$, the length of the permeable wall region along x' is $a_2' = 694.3\,\mu\text{m}$ and the half width is $b' = 229.5\,\mu\text{m}$.

3.2 Experimental setup

A schematic of the experimental setup is shown in Fig. 2b. An upright Olympus BX43 microscope with an multiphoton Olympus XLPlan N water immersion objective with magnification M = 25× and numerical aperture NA = 1.05 was used in the experiments. A water immersion objective was chosen to minimize spherical aberrations, see e.g. Wereley and Lueptow (2015). For the streakline visualizations in Fig. 3a, b, a dry Olympus PlanC N objective with M = 10×, NA = 0.25 objective was used, and a mercury lamp from Olympus (U-HGLGPS) was used to illuminate the particles. A Litron npiv Nd:YAG laser with wavelength



(a)



(b)

Fig. 2 **a** The hydrodynamic particle separation microchip with global coordinate system (x', y'). The separation unit is located in the center of the channel. Channel height is $h = 90\,\mu\text{m}$, the trilobite width $2b' = 459\,\mu\text{m}$ and the length is $a' = 1137\,\mu\text{m}$. The channel width in the main channel is $2B = 10\,\text{mm}$ and the length is $A = 30\,\text{mm}$. Inlet and permeate outlet are pressure regulated. The outlet downstream is an atmospheric pressure outlet. Permeate outlet, pillars and bluff body are not to scale. **b** Experimental setup for the flow field measurements. Flow through the system was driven by a pressure system by pressurizing the inlet and permeate outlet reservoirs. The pressure in the concentrate reservoir was atmospheric. A scale was used to measure the volumetric flux. Particle images were captured through a water immersion objective onto a CCD chip. A Nd:YAG laser was used to illuminate the fluorescent particles for the PIV measurements, and a mercury lamp was used for the streakline visualizations

532 nm was used to illuminate the particles for the PIV measurements. This laser has a double cavity which enables a short time difference between the two successive pulses. Image pairs were captured with a pco.4000 CCD chip camera. An optical arm was used to guide the laser beam safely to the microscope. Fluorospheres tracer particles from Life Technologies with nominal diameter $d_p = 1\,\mu\text{m}$ were mixed with the working fluid, which was distilled water, to a concentration of 1.14×10^{-5} by volume. The excitation and emission maxima of these particles are $\lambda_{\text{ex}} = 540\,\text{nm}$ and $\lambda_{\text{em}} = 560\,\text{nm}$, respectively. 2.8 pixels on the CCD array resolved these particles, which means that they were sufficiently resolved.

Pulseless flow through the system was driven by pressurized air via a pressure system from Fluigent. PTFE tubing from IDEX connected the reservoirs to the chip and syringe filters from Sartorius with 5 µm pore size prevented unwanted particles such as dust from entering into the channels. The pressure in the concentrate reservoir was atmospheric. Surfactant Triton-X from Sigma Aldrich was added to the working fluid to reduce the formation of bubbles and particle agglomeration to the walls and coverslip surface. The ensemble PIV algorithm described in Kolaas (2016) was used to extract the velocity fields from the raw image data. The subwindows were 128 pixels wide and overlapped by 75%. Multipass was used to increase the spatial resolution, which was 5 µm.

3.3 Calibration and validation

Prior to the velocity measurements, we calibrated the setup by measuring flow in a duct and validated the results by comparing them to the analytical solution, see White (1991). The calibration channel in Fig. 2a was used for this. To minimize the influence from particles out of focus or slightly out of focus on the velocity measurements, a background intensity image was subtracted from each image used in the ensemble PIV algorithm, see Cowen and Monismith (1997). The main result of the calibration measurements is that the measured u-velocities are 95% of the analytical u-velocity. The 5% discrepancy is due to contributions from particles out of focus or slightly out of focus. For details, see Mossige et al. (2015).

3.4 Experimental procedure

The pressure difference between the inlet and the permeate outlet $\Delta p = (p_{\text{in}} - p_p)/p_{\text{in}}$ determines the position of the saddle point: a small Δp results in an upstream saddle point and thus a small T_p, and a large Δp results in a downstream saddle point and a thus a large T_p. We performed measurements for two different positions of the saddle point. These were 30 µm upstream and 90 µm downstream of 4 in Fig. 1b. The upstream saddle point is marked by the 'X', and the downstream saddle point is marked by the '+'. For each of the saddle points, we performed velocity measurements for 3 different Reynolds numbers ($Re = UL/\nu$), to study how the flow layer thicknesses T_p and T_{bl} depend on the Reynolds

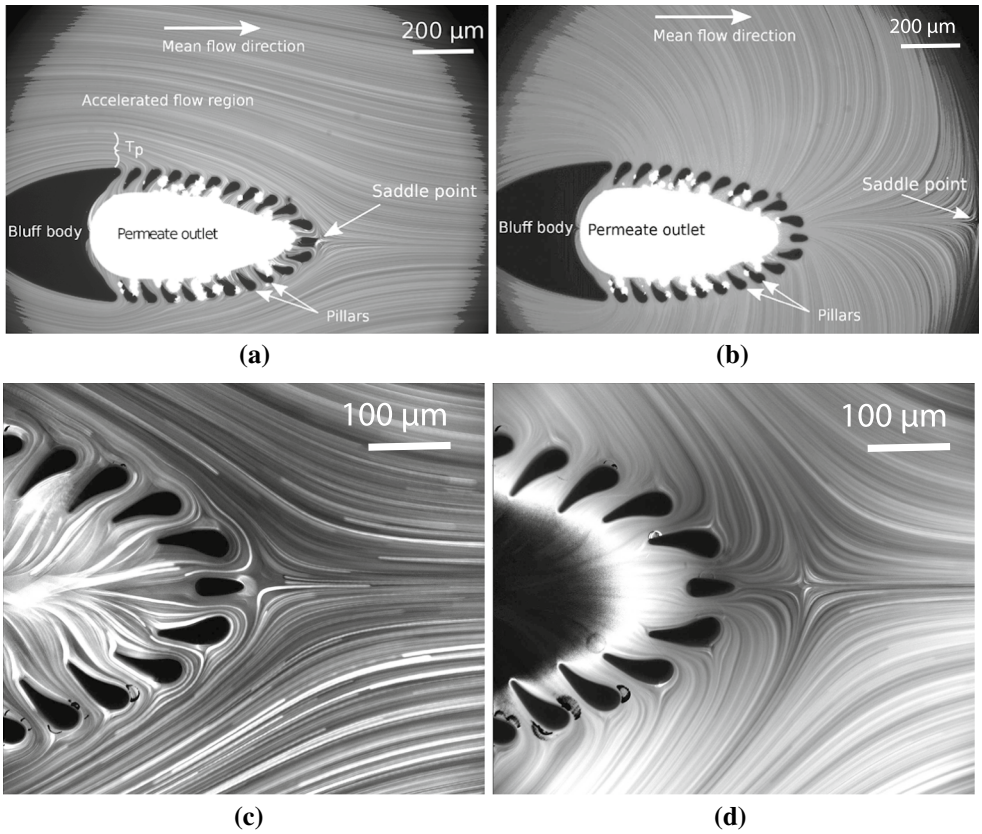


Fig. 3 **a**, **b** Streaklines obtained with tracer particles show different working modes of the separation unit. In **a**, the unit is operated like a crossflow filter. Here, the saddle point is in an upstream position which results in a flow that is parallel to the permeable wall. In **b**, the saddle point is moved downstream, and the streaklines are normal to the permeable wall. Therefore, separator is operated like a dead-end filter. In **b**, T_p is larger than the field-of-view of the 10x-objective. In both **a** and **b**, the flow is symmetric about the major axis and $Re = 2.8$. The white dots are agglomeration of particles. Flow visualizations show that these particles do not influence the flow. However, they deteriorate the light signal from the particles in the flow and therefore new, clean chips without stationary particles were used for the PIV measurements. **c**, **d** Streakline visualizations around the **c** upstream ($Re = 2.8$) and **d** downstream ($Re = 29$) saddle points. Mean flow is from *left* to *right*

number. For the Reynolds number, the minor axis b' was chosen as the characteristic length L, see Fig. 2, and the bulk velocity U_{bulk} as the characteristic velocity U. The kinematic viscosity ν is that if of the working fluid, i.e. 1.002×10^{-6} for distilled water. U_{bulk} is based on the total flux through the system and the cross-sectional area, $2Bh$. The three Reynolds numbers were $Re = 2.8$, $Re = 29$ and $Re = 58$.

We found T_{bl} for the upstream saddle point position only. This is because the separator works like a dead-end filter when the saddle point is in the downstream position in which case wall normal forces are assumed not to affect the separation of particles. In total, 53 image pairs were used to calculate each velocity field for $Re = 58$. When the 53 image pairs had been captured, the inlet reservoir had emptied and 53 was therefore the maximum possible number of image pairs. For $Re = 2.8$ and $Re = 29$, the inlet reservoir emptied more slowly which allowed us to collect a total of 119 image pairs that were used to calculate the velocity field.

4 Results

4.1 Permeate layer thickness T_p

Streakline visualizations of the flow around the separation unit is shown in Fig. 3 for $Re = 2.8$. In (a), the saddle point is in an upstream position. The majority of the streaklines are approximately parallel to the separation unit. Therefore, the unit is operated as a crossflow filter. Inside the permeate layer T_p, the streaklines are directed inwards, toward the permeate outlet. In (b), the saddle point is in a downstream position. The streaklines in the permeable wall region are normal to the permeable wall. Therefore, the unit is operated as a dead-end filter. The visualizations illustrate how the saddle point position dictates the thickness T_p. When the saddle point is in an upstream position as in Fig. 3a, T_p is small, and when the saddle point is in a downstream position as in Fig. 3b, T_p

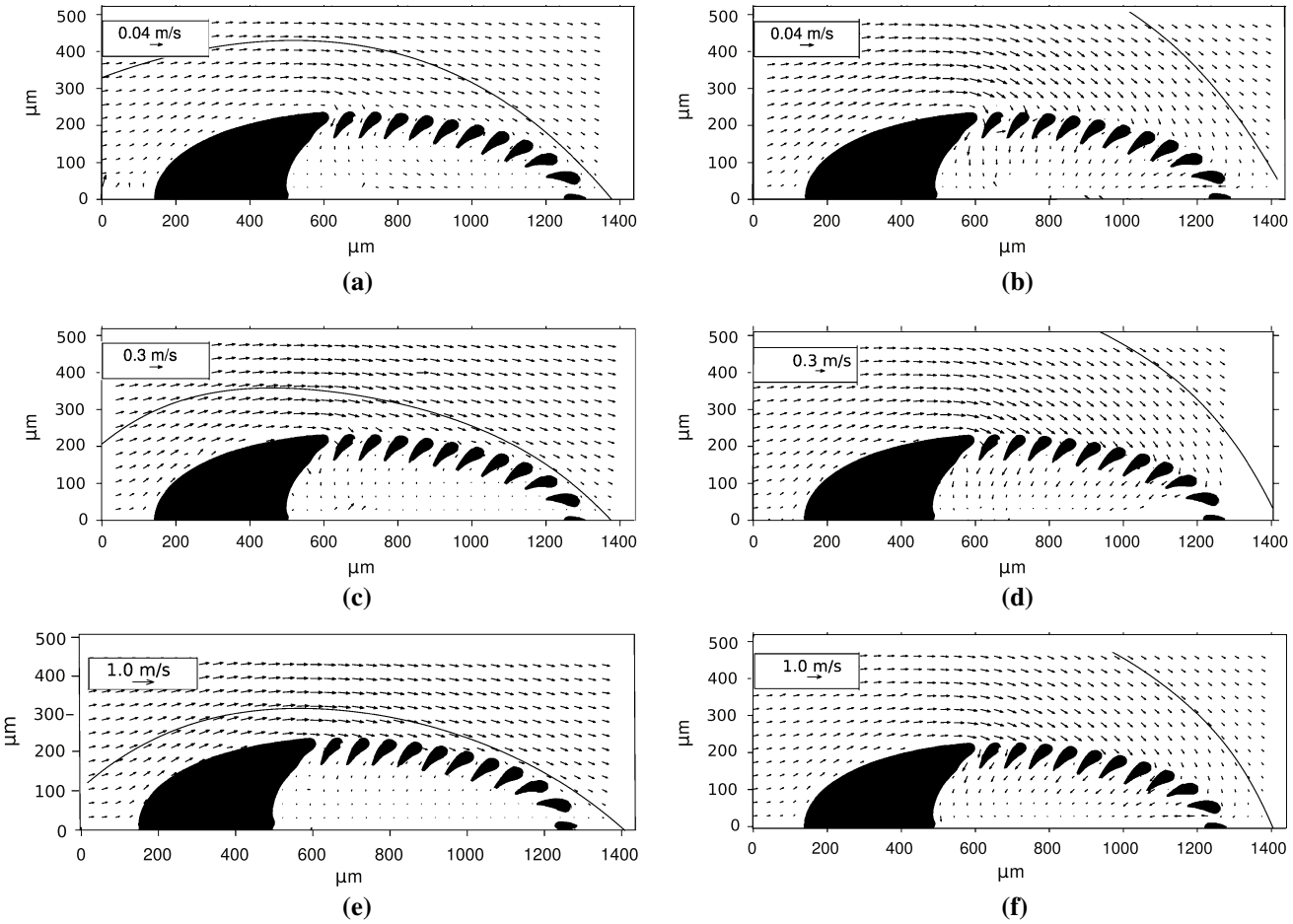


Fig. 4 Velocity vectors for $Re = 2.8$ (**a**, **b**), $Re = 29$ (**c**, **d**), $Re = 58$ (**e**, **f**). The *solid line* is the permeate thickness T_p. For the upstream saddle point, T_p decreases when the Reynolds number increases. For the downstream saddle point, T_p changes little with the Reynolds number. Mean flow is from *left* to *right*

is large. In both cases, the flow field is symmetric about the major axis.

Figure 3c, d is a streakline visualization of the (c) upstream and (d) downstream saddle points described in Fig. 1. From the visualizations, we see that T_p increases when the saddle point is moved from the upstream position in (c) to the downstream position in (d).

Based on the hydraulic resistance of the tubing, see e.g. Bruus (2008), and the flow rate of permeate Q_p and concentrate Q_c, we estimated the inlet and outlet pressures on the chip for the upstream saddle point position. For the three Reynolds numbers, $Re = 2.8$, $Re = 29$ and $Re = 58$, the estimated inlet pressures are $p_{\text{in}} = 0.07$ bar, $p_{\text{in}} = 0.50$ bar and $p_{\text{in}} = 1.17$ bar, respectively. The corresponding permeate outlet pressures are $p_p = 0.04$ bar, $p_p = 0.26$ bar and $p_p = 0.58$ bar. For the concentrate outlet pressure, these values are $p_c = 0.01$ bar, $p_c = 0.13$ bar and $p_c = 0.27$ bar. The pressure drop between inlet and permeate outlet $\Delta p = \left(p_{\text{in}} - p_p\right)/p_{\text{in}}$ corresponds to the pressure drop needed to overcome the friction in a 0.13 m long channel with width and height equal to that of the main channel, see Fig. 2a. This is much longer that the distance from the inlet to the permeate outlet on the chip, which is 0.015 m. The reason for this discrepancy is that most of the pressure is lost to friction in the branching channels, upstream of the main channel, where the hydraulic resistances are much higher than in the main channel.

In Fig. 4, the velocity field for the different flow configurations is shown. The flows for the downstream saddle point on the right are directed much more inwards, toward the permeate outlet, than the flow for the upstream saddle point position. The solid lines indicate the permeate layer thickness, which increases when the saddle point is moved downstream, a result which is confirmed by the visualizations in Fig. 3. From the plots, it is seen that changes in the flow rate have a strong impact on T_p for the upstream saddle point: an increase in the flow rate results in a thinning of the permeate layer T_p. For the downstream saddle point, changes in the flow rate have only a weak impact on the permeate layer. For the plots in Fig. 4, T_p was found from

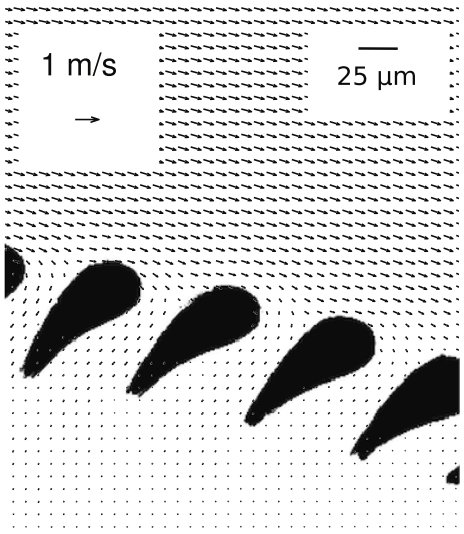


Fig. 5 Vector plot for $Re = 58$ and upstream saddle point position. Velocity field around the separator shows no sign of flow separation

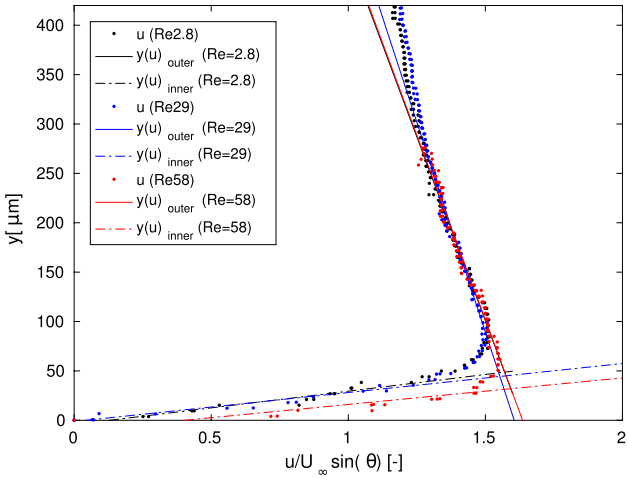


Fig. 6 Streamwise velocity data for $Re = 2.8$ (*black dots*), $Re = 29$ (*blue dots*) and $Re = 58$ (*red dots*) and linear fit to the boundary layer flow (*dotted lines*) and the outer flow (*solid lines*). The boundary layer thickness is found from the intersection of these lines. The profiles were taken at $\tilde{x} = 0.408$. The velocities were normalized by the potential flow velocity at infinity around a circular cylinder, $\sin(\theta)U_\infty$ (color figure online)

streamlines and from streakline visualizations. The streamlines were extracted from the PIV-obtained velocity fields.

Consider the flow field for $Re = 58$ and upstream saddle point in Fig. 5. From the vector field, no sign of flow separation is seen. This is probably due to the permeate suction force, which is known to stabilize flows and suppress flow separation (Kay 1953). Without suction, flow separation around cylinders is predicted to occur, provided that the flow has inertia (Schlichting 1968). A stable flow is desirable from an operational point of view because it eases the prediction of the particle tracks and therefore the size of the particles that ends up in the concentrate and permeate, respectively, i.e. the cut-off size.

4.2 Boundary layer thickness T_{bl}

Figure 6 shows u-velocity data at $\tilde{x} = 0.408$ for different Reynolds numbers. The velocities were normalized by the potential flow velocity at infinity around a circular cylinder, $\sin(\theta)U_\infty$, where θ is the orientation of the local coordinate system relative to a global coordinate system, see Fig. 1b. The bulk velocity was used to calculate the flow velocity at infinity, $U_\infty = C \cdot U_{\text{bulk}}$. A parabolic flow profile was assumed, hence $C = 3/2$ and $U_\infty = 3U_{\text{bulk}}/2$. The thickness T_{bl} was found from the intersection of the linear velocity gradients of the inner flow close to the wall, known as the boundary layer flow, with the outer flow far away from the wall. This method is similar to the approach by Tobias et al. (1952) for concentration boundary layers. T_{bl} was found from the streamwise velocity profiles at 17 different x-positions along the geometry, measured in the wall normal direction y.

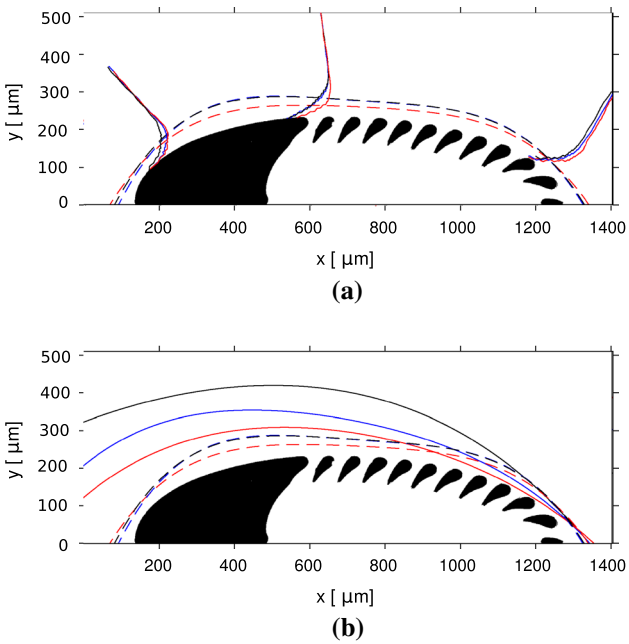


Fig. 7 Flow layers and u-velocity profiles for the upstream saddle point position for $Re = 2.8$ (*black*), $Re = 29$ (*blue*) and $Re = 58$ (*red*). **a** Boundary layer thickness T_{bl} (*dotted line*) and u-velocity profiles (*solid lines*). T_{bl} is calculated from the shape of the u-velocity profiles. Changes of T_{bl} along the permeable wall are small and within the measurement accuracy. **b** Boundary layer thickness (*dotted lines*) and permeate thickness T_p (*solid lines*). Except far downstream, T_{bl} is smaller than T_p. Therefore, if normal forces are to influence the separation of particles, this will occur inside the permeate layer. Mean flow is from *left* to *right*. The maximum u-velocity for $Re = 58$ is 1.6 times the freestream velocity around a circular cylinder, $U_\infty \cdot \sin\theta$ (color figure online)

Table 1 Fraction of the incoming flow that ends up as permeate in % (Q_p), permeate thickness T_p, boundary layer thickness T_{bl} and theoretical boundary layer thickness $T_{bl,th}$ at $\tilde{x} = 0.408$ for different Reynolds numbers (Re#)

Re#	Saddle point position					
	Upstream				Downstream	
	Q_p (%)	T_p (μm)	T_{bl} (μm)	$T_{\mathrm{bl,th}}$ (μm)	Q_p (%)	T_p (μm)
$Re = 2.8$	6	184	45	110	12	438
$Re = 29$	2	118	44	34	12	406
$Re = 58$	2	78	29	24	9	N/A

Parts of the flow layer is outside of the Field-of-View of the objective lens for the highest flow rate and downstream saddle point, hence the N/A in the table

The u-velocity profiles and the boundary layer thickness T_{bl} are plotted in Fig. 7a. An increase in the Reynolds number from $Re = 29$ to $Re = 58$ results in a thinning of the boundary layer. The steep velocity gradients for $Re = 58$ result in a boundary layer that is thinner than for $Re = 29$. Between $Re = 2.8$ and $Re = 29$, the change of T_{bl} is within the accuracy of the experimental setup. The boundary layer thickness depends on the streamwise coordinate $\tilde{x}$ as well as on the Reynolds number, $T_{\mathrm{bl}} = T_{\mathrm{bl}}(\tilde{x}, Re)$ up to about $\tilde{x} = 0.408$. The boundary layer grows for $\tilde{x}$ <0.240, which corresponds to 1 to 2 in Fig. 1b, and shrinks for 0.240< $\tilde{x}$ < 0.408 (between 2 and 3). Changes of T_{bl} along the permeable wall are small and within the measurement accuracy. This result is in line with the theory for boundary layers with suction (Tilton and Cortelezzi 2015). In Fig. 7b, T_{bl} (dotted) is compared to T_p (solid lines). Except far downstream, T_{bl} is smaller than T_p. This means that if normal forces are to affect the separation of particles, this will occur inside the permeate layer.

In Table 1, T_{bl} is listed at $\tilde{x} = 0.408$ together with T_p. The small variation in T_{bl} between $Re = 2.8$ and $Re = 29$ is within the measurement uncertainty of the setup. When the Reynolds number increases from $Re = 29$ to $Re = 58$, the thickness T_{bl} decreases from 44 to 29 μm, a significant decrease. When inertia is assumed to dominate over viscosity, a boundary layer approximation could be used to estimate a theoretical boundary layer thickness from a characteristic length L and Re, $T_{bl,th} \approx L/\sqrt{Re}$, see e.g. Schlichting (1968). With $L = b'$, this thickness becomes $T_{bl,th} \approx b'/\sqrt{Re} = \sqrt{\nu b'/U_\infty}$. In Table 1, the theoretical thickness $T_{bl,th}$ is compared to the thickness obtained with experiments T_{bl}. As seen from the table, the boundary layer thickness approaches the value predicted by theory when the Reynolds number increases. It is also seen that theory fails to predict the thickness for the lowest Reynolds number. This is to be expected as the boundary layer approximation does not apply when inertia does not dominate over viscosity as is the case for $Re = 2.8$.

When the flow rate decreases, the fraction of the total fluid that ends up as permeate increases, see Q_p in Table 1. This is in agreement with the observation of Dong et al. (2011). The reason for this, evidenced by our experiments, is that the normalized u-velocity profiles are almost identical over the range of flow rates we studied, see Fig. 6, except in the boundary layer. Since Q_p is the velocity integral over T_p, and the normalized velocities change little with the flow rate, the increase of Q_p with lower flow rates is mainly due to the thickening of T_p.

Moving to saddle point from the upstream to the downstream position also leads to an increase of Q_p, see Table 1. While the cross-section of the Trilobite™ unit is less than 5% of the channel width, as much as 12% of the incoming fluid ends up as permeate when the saddle point is in the downstream position. This means that the separator is a promising concentrator. The total flux was found from the sum of the concentrate flux Q_c plus the flux of permeate Q_p. Q_c was found by sampling the weight of the concentrate reservoir, see schematic of the setup in Fig. 2b. Q_p was found by integrating the u-velocity, found from the PIV measurements, over the thickness T_p. Parts of the flow layer is outside of the Field-of-View of the objective lens for the highest flow rate and downstream saddle point, hence the N/A in the Table 1. The reason why the weight of the inlet reservoir was not used to calculate the total flux was that the reservoir was too heavy for the scale.

5 Conclusion

We have characterized the permeate flow layer and the boundary layer for different flow configurations by varying the Reynolds number and the position of a saddle point. For the downstream saddle point, the thickness of the permeate layer changes little with the Reynolds number. For the same saddle point position, the separator shows promising concentration characteristics. For the upstream saddle point, the permeate flow layer decreases with increasing Reynolds number. This is mainly due to a decrease of the permeate flow layer T_p. For sufficiently large Re, it should therefore be possible to create a permeate flow layer whose thickness is smaller than the pore size l of the permeable wall, $T_p < l$. This would enable particle separation entirely determined by hydrodynamics, and therefore a clog-free configuration.

The highest Reynolds number we were able to achieve before the cover glass broke due to high pressures was

58. Future designs should therefore focus on the development of chips that can handle higher flow rates to see if it is possible to achieve $T_p < l$. A numerical model that can simulate Reynolds numbers above 58 could also be useful.

We observed no sign of flow separation, which is beneficial for the prediction of the cut-off size of particles.

Acknowledgements This project was funded by Trilobite and The Research Council of Norway–Project Number 232148. Support was also received from the Norwegian micro- and nanofabrication Facility (NORFAB) infrastructure project.

Appendix: Calculation of the total flux

The total flux, $Q_{\text{tot}} = Q_p + Q_c$, is slightly changed when the saddle point is moved from the upstream to the downstream position. The change, however, is less than 2% for the lowest flow rate, corresponding to $Re = 2.8$, and less than 1% for the intermediate flow rate ($Re = 29$), and could be neglected. The permeate flow rate Q_p for $Re = 58$ and downstream saddle point position is unknown because parts of the permeate flow layer is outside the field-of-view of the objective lens. Therefore, the total flow rate is unknown. But since Q_{tot} changes by 1% for $Re = 29$ when the saddle point is moved between the upstream and downstream position, we assume that this is also true for the highest flow rate ($Re = 58$). We therefore assumed that the total flux Q_{tot} for the downstream saddle point was the same as for the upstream saddle point, which we knew, and calculated the permeate flux from $Q_p = Q_{\text{tot}} - Q_c$.

References

Bruus H (2008) Theoretical microfluidics. Oxford master series in condensed matter physics. Oxford University Press, New York

Cowen EA, Monismith SGM (1997) A hybrid digital particle tracking velocimetry technique. Exp Fluids 22:199–211. doi:10.1007/s003480050038

Dong T, Yang Z, Su Q, Tran NM, Egeland EB, Karlsen F, Zhang Y, Kapiris MJ, Jakobsen H (2011) Integratable non-clogging microconcentrator based on counter-flow principle for continuous enrichment of CaSki cells sample. Microfluid Nanofluid 10(4):855–865. doi:10.1007/s10404-010-0717-x

Grandison AS, Lewis MJ (1996) Separation processes in the food and biotechnology industries: principles and applications. Woodhead Publishing Limited, Cambridge

Hönsvall BK, Altin D, Robertson LJ (2016) Continuous harvesting of microalgae by new microfluidic technology for particle separation. Bioresour Technol 200:360–365. doi:10.1016/j.biortech.2015.10.046

Hood K, Kahkeshani S, Di Carlo D, Roper M (2016) Direct measurement of particle inertial migration in rectangular microchannels. Lab Chip. doi:10.1039/C6LC00314A

Jäggi RD, Sandoz R, Effenhauser CS (2007) Microfluidic depletion of red blood cells from whole blood in high-aspect-ratio microchannels. Microfluid Nanofluid 3(1):47–53. doi:10.1007/s10404-006-0104-9

Jhansi SC, Mishra SK (2013) Wastewater treatment and reuse: sustainability options. Cons J Sustain Dev. doi:10.7916/D8JQ10Q1

Kay JM (1953) Boundary-layer flow along a flat plate with uniform suction. Technical report, Mech. E. Cambridge University Engineering Laboratory

Karimi A, Yazdi S, Ardekani AM (2013) Hydrodynamic mechanisms of cell and particle trapping in microfluidics. Biomicrofluidics 7(2):021501. doi:10.1063/1.4799787

Kolaas J (2016) Getting started with hydrolabPIV v1.0. Preprint series research report in mechanics. http://urnnbno/URN:NBN:no-53997

Kolaas J, Jensen A, Mielnik M (2013) Visualization and measurements of flows in micro silicon y-channels. Eur Phys J E 36(2):1–11. doi:10.1140/epje/i2013-13019-x

Lenshof A, Laurell T (2010) Continuous separation of cells and particles in microfluidic systems. Chem Soc Rev 39:1203–1217. doi:10.1039/B915999C

Lim E (2014) Inertio-elastic focusing of bioparticles in microchannels at high throughput. Nat Commun 5: doi:10.1038/ncomms5120

Meinhart CD, Wereley ST, Gray MHB (2000) Volume illumination for two-dimensional particle image velocimetry. Meas Sci Technol 11(6):809. http://stacks.iop.org/0957-0233/11/i=6/a=326

Meinhart CD, Wereley ST, Santiago JG (1999) Piv measurements of a microchannel flow. Exp Fluids 27(5):414–419. doi:10.1007/s003480050366

Mielnik MM, Ekatpure RP, Saetran LR, Schonfeld F (2005) Sinusoidal crossflow microfiltration device-experimental and computational flowfield analysis. Lab Chip 5:897–903

Mossige E, Jensen A, Mielnik M (2015) Characterization of the trilobite hydrodynamic particle separation microchip with μpiv. In: Proceedings of the 11th international symposium on particle image velocimetry—PIV2015, Santa Barbara, CA, USA, September 14–16, 2015

Nabeth S Jeremy, Chigullapalli S, Alexeenko AA (2010) Knudsen force modeling in application to microsystems. Technical report, School of Aeronautics and Astronautics Faculty Publications. Paper 26. doi:10.2514/6.2010-5054

Pamme N (2007) Continuous flow separations in microfluidic devices. Lab Chip 7:1644–1659. doi:10.1039/B712784G

Park JS, Choi CK, Kihm KD (2004) Optically sliced micro-PIV using confocal laser scanning microscopy (CLSM). Exp Fluids 37(1):105–119. doi:10.1007/s00348-004-0790-6

Rivet C, Lee H, Hirsch A, Hamilton S, Lu H (2011) Microfluidics for medical diagnostics and biosensors. Chem Eng Sci 66(7):1490–1507. doi:10.1016/j.ces.2010.08.015

Saffman PG (1965) The lift on a small sphere in a slow shear flow. J Fluid Mech 22:385–400. doi:10.1017/S0022112065000824

Schlichting H (1968) Boundary-layer theory, 6th edn. McGraw-Hill series in mechanical engineering. McGraw-Hill, New York

Sugaya S, Yamada M, Seki M (2011) Observation of nonspherical particle behaviors for continuous shape-based separation using hydrodynamic filtration. Biomicrofluidics 5(2):024103. doi:10.1063/1.3580757

Svanes K, Zweifach B (1968) Variations in small blood vessel hematocrits produced in hypothermic rats by micro-occlusion. Microvas Res 1(2):210–220. doi:10.1016/0026-2862(68)90019-8

Tilton N, Cortelezzi L (2015) Stability of boundary layers over porous walls with suction. AIAA J 53(10):2856–2868

Tobias CW, Eisenberg M, Wilke CR (1952) Fiftieth anniversary: diffusion and convection in electrolysisa theoretical review. J Electrochem Soc 99(12):359C–365C. doi:10.1149/1.2779636. http://jes.ecsdl.org/content/99/12/359C.full.pdf+html

Wereley ST, Lueptow RM (2015) Microscopy u: Water immersion objectives. http://www.microscopyu.com/articles/optics/waterimmersionobjectives.html

White FM (1991) Viscous fluid flow. McGraw-Hill series in mechanical engineering. McGraw-Hill, New York

WHO/UNICEF Joint Monitoring Programme for Water Supply and Sanitation (2004) Meeting the MDG drinking water and sanitation target: a mid-term assessment of progress. http://apps.who.int/iris/bitstream/10665/43021/1/9241562781.pdf?ua=1

WWAP (United Nations World Water Assessment Programme) (2015) The United Nations world water development report 2015: water for a sustainable world. http://unesdoc.unesco.org/images/0023/002318/231823E.pdf

Yamada M, Seki M (2005) Hydrodynamic filtration for on-chip particle concentration and classification utilizing microfluidics. Lab Chip 11:1233–1239

Zhu T, Ye W, Zhang J (2011) Negative Knudsen force on heated microbeams. Phys Rev E 84:056,316. doi:10.1103/PhysRevE.84.056316

Zhu T, Ye W (2010) Origin of knudsen forces on heated microbeams. Phys Rev E 82:036,308. doi:10.1103/PhysRevE.82.036308